ARCHIVE OF MECHANICAL ENGINEERING

DOI: 10.24425/ame.2024.152617 2024, Vol. 71, No. 4, pp. 547–560

Nina YURCHENKO [1], Pavlo VYNOGRADSKYY [1], Roman PAVLOVSKYY

Improvement of the airfoil lift and drag characteristics using plasma-efficient flow control

Received 28 July 2024, **Revised** 10 November 2024, **Accepted** 25 November 2024, **Published online** 6 December 2024

Keywords: aerodynamics, interdisciplinary research, flow restructuring, lift and drag coefficients

Flow control is studied to improve the aerodynamic performance of an aerofoil. The authors use a strategy for maintaining the near-wall flow structure with a given spatial scale, developed within the framework of interdisciplinary research. The proposed active flow control method is based on the application of spanwise arrays of mechanical, thermal, or plasma vortex generators. The latter have been found most versatile and efficient for the formulated goal. Aerodynamic coefficients measured in the specified wind tunnel are discussed for a 12.5% supercritical airfoil model. The model is controlled by a spanwise array of pulsating high-voltage plasma discharges. This multi-actuator system allows for applying a sufficient number of control parameters such as pulse duration and repetition rate, the distance between the neighboring actuators (space scale of generated disturbances), and the plasma array location along the airfoil chord. Measurements in the range of Reynolds numbers of $\mathrm{Re_c} = (3 \div 7) \times 10^5$ showed that maximal lift coefficient $\mathrm{C_{L\,max}}$ grows up to 10% and the stall angle increases by 1.5°–3.5°, which is accompanied by drag reduction by up to 7%.

1. Introduction

The idea of energy-efficient flow control stems from the studies of high-speed marine animals whose skin features are thoroughly selected and perfected by evolution [1–4], Fig. 1. Relevant engineering realizations were first designed in the form of riblets to provide passive flow control. It was shown that triangular riblets and spanwise arrays of mechanical vortex generators can enhance the heat transfer by ~ 30% [5–7] as well as reduce drag (see, e.g., [8–11]).

✉ Nina YURCHENKO, e-mail: nina.yurchenko@gmail.com

[1] Institute of Hydromechanics, National Academy of Sciences of Ukraine, Laboratory for Advanced Aerodynamics and Interdisciplinary Research, Kyiv, Ukraine

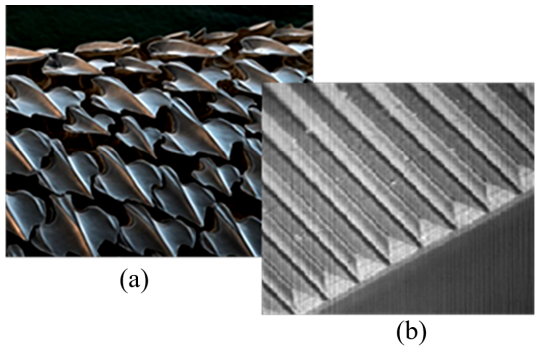

Fig. 1. Spanwise-regular structure of the surface: (a) shark denticles [4], (b) riblets

Next, active flow control methods were developed and tested using pneumatic, acoustic, and thermal vortex generators regularly spaced in a spanwise direction. Fig. 2 shows an example of a numerically evaluated flow field restructured with an array of thermal vortex-generators [12, 13]. They work similarly to mechanical ones, initiating the development of a system of streamwise vortices with a given scale that change fluid transport in a boundary layer [14, 15].

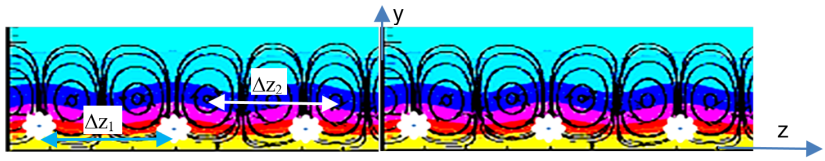

Fig. 2. Schematic view of the boundary layer cross-section structure over a spanwise-regular array of thermal vortex-generators

The multidisciplinary approach to investigations which connected the essential biological findings and plasma physics instrumentation resulted in the most beneficial fluid dynamic solution. It is the design of spanwise arrays of localized plasma vortex generators energized either by a microwave field [16] or by high-voltage sparks [17]. Single spark discharges were studied basically in supersonic flows [18–20]. The impact of the array of discharges in transonic flows, investigated in these works, showed a favorable effect greater than that of mechanical systems. This effect was supplemented with such advantages as:

- the possibility to operate in a remote mode depending on a method of energy deposition to plasma actuators, e.g., using microwave radiation;
- the control factor applied directly to the flow keeps the surface smooth;
- greater versatility in the pulsating mode operation due to the use of many control parameters.

Similar investigations were repeated recently in UAV flight tests in the framework of the same strategy of multiple vortex generation along the airfoil span that increased

maximum lift capability [21]. The physical mechanisms of a single spark discharge impact on the quiescent air are discussed in [22].

In [16], adequacy of the flow response to the scale of generated streamwise vortices is assessed by the commensurability of scales of introduced and naturally developing disturbances in the flow, $\Delta z_1 = \Delta z_2$ (Fig. 2) or, e.g., $\Delta z_1 = 0.5\Delta z_2$. This condition provides certain stability of the organized vortical motion and thus has a sustainable impact on integral flow characteristics. The measure of plasma impact on the flow is evaluated based on the characteristics of the aerodynamic performance, lift and drag coefficients as well as pressure redistribution around a model. The conclusions are verified with the results of numerical modeling, e.g., flow fields over controlled models similar to those of Fig. 2. In the case of an incompatible scale of generated disturbances, the flow field is seen as an irregular and unstable structure.

The impact of multi-discharge arrays on aerodynamic performance has been studied numerically and experimentally taking into account the correlation between basic flow and control parameters. Aerodynamic coefficients and pressure fields were measured for models of circular cylinders in a crossflow, turbine blades, and airfoils. In this paper, measured lift and drag coefficients are discussed for airfoil models controlled by a system of spanwise-regular spot plasma discharges with changeable parameters at various Reynolds numbers.

2. Aerodynamic Complex for Interdisciplinary Research (ACIR)

2.1. Wind tunnel

ACIR includes the horizontal atmospheric pressure wind tunnel 6250 mm long and the data acquisition, processing and control system (DAS) [21]. Fig. 3 shows the general arrangement of the wind tunnel. The intake provides smooth

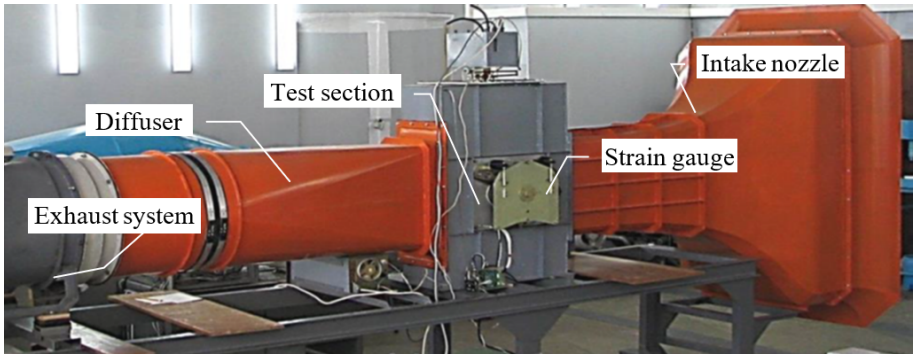

Fig. 3. Wind tunnel with the systems for automated measurements of aerodynamic forces and pressure distributions over a model: closed-return type; elliptical test section 75×42×90 cm; U_0 = 1–65 m/s; external 3-component strain gauge balance, precision – 20 mN; resolution – 2 mN

air entrance into the wind tunnel from outside, where low-velocity reversed flow is available. The nozzle with an 11.2:1 contraction ratio delivers air from the turbulence-settling chamber with the protective and anti-turbulence screens located in series.

2.2. Measurement system

ACIR is equipped with the 3-component strain gauge balance (Fig. 4) to measure aerodynamic loads on the model in a vertical plane: lift, drag, and pitch moment. On the floating plate attached to the base via elastic hinges, a play-free worm-gear pitch mechanism is located to position the model at any angle. The mechanism is controlled by commands from the DAS. The model's angle to the free-stream velocity is measured using an incremental encoder. On the floating plate of the balance, a block with 25 pressure sensors is installed to measure pressure distribution over the model surface.

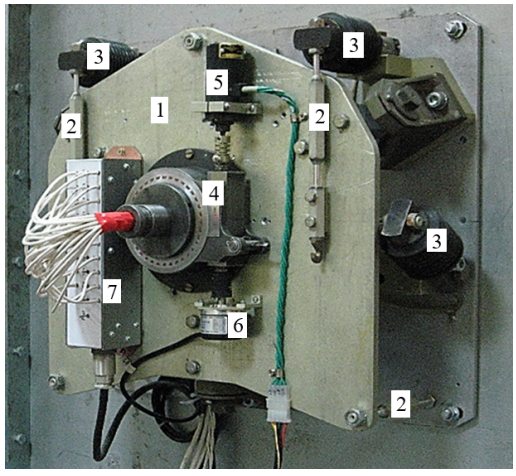

Fig. 4. Three-component strain gauge balance. 1 – floating plate;
2 – elastic hinges; 3 – strain gage transducers;
4 – worm-gear pitch mechanism; 5 – pitch drive stepper motor;
6 – incremental encoder; 7 – pressure sensor block (25 sensors)

The panel connects the DAS with the strain gauge, the pressure sensors block, the pitch control mechanism, the incremental encoder, the constant temperature anemometer, and auxiliary devices. The DAS performs processing of all analog signals of dynamic pressure and pressure distribution as well as control of the fan, the pitch mechanism, and the system of plasma discharges.

3. Multi-spark plasma array for flow control

The analysis of published data on plasma-assisted flow control have shown that electric spark actuators can be successfully used for generation of the spanwise-regular disturbances of the type discussed here in Section 1. Thus, the multi-discharge plasma system for flow control was designed to satisfy the following requirements:

- the possibility to be mounted at different downstream locations of the model keeping the surface smooth;
- discharge initiation at a certain distance from the surface without its noticeable heating;
- stability of a chosen pulse operation mode;
- controllability of temporal characteristics.

3.1. Multi-electrode actuators

The spark discharge generation system consists of the multi-electrode plasma array and the developed high-voltage power source. Initially, it was tested to determine an optimal discharge gap length to design an efficient and stable system.

Several kinds of multi-electrode actuators were developed for flow-control purposes. Fig. 5 shows the plasma actuator in the form of an insert in the model body. It consists of 46 electrodes flush-mounted in the insulating plate. The electrodes are 3.5 mm in diameter located at 0.5 mm distance from each other. The actuator insert is 200 mm long, which is equal to the airfoil model span. Grounded central and end electrodes are mounted through the insulator to provide an electrical connection shown in Fig. 4. A high-voltage pulse applied to the terminal electrodes ignites 45 discharges between neighboring electrodes. It corresponds to the scale of generated vortices, $\Delta z = 4$ mm, which is used in the present study; another option of $\Delta z = 10$ mm is realized in a different insert.

An optical spectroscopy technique was used to investigate emission in different discharge modes. No electrode material spectral lines were found. It implies that erosion of metal particles from the electrodes doesn't affect the properties of spark discharge plasma.

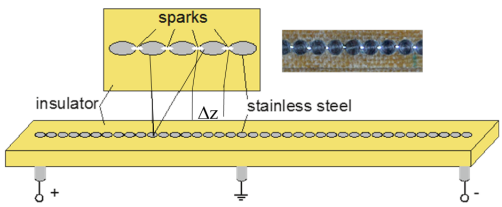

Fig. 5. Multi-electrode plasma actuator

4. Airfoil test models with arrays of plasma discharges

It was shown earlier [17] that the developed energy-efficient flow-control strategy worked well for separated flows, e.g., around a circular cylinder in a cross flow. The present study is focused on flow control around the "Supercritical Airfoil Profile" (SAP) (Figs. 6, 7) which was designed to mitigate the unfavorable effect of flow separation. Numerical and experimental investigations were carried out over an airfoil with 12.5% relative thickness which was similar to the NASA TP 3579 used in Cessna Executive Jet with 12.0% relative thickness.

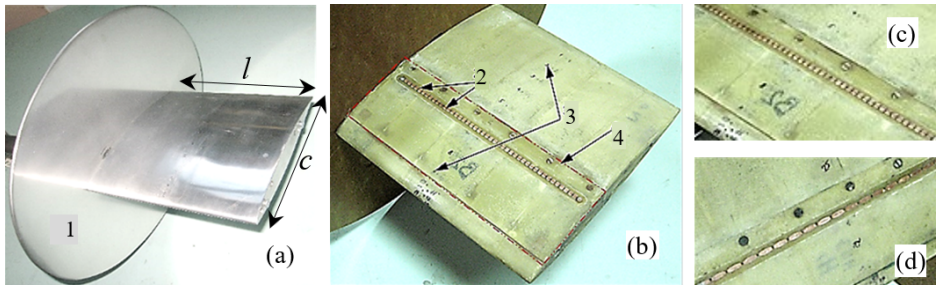

Fig. 6. Airfoil SAP2 models: uncontrolled (a), controlled (b-d) with $\Delta z_1 = 4$ mm (b, c) and $\Delta z_1 = 10$ mm (d): 1 – endplate; 2 – discharge gaps; 3 – pressure taps; 4 – plasma insert

A smooth model was used as the baseline for aerodynamic performance comparisons. The SAP1 models are equipped with the plasma arrays mounted across their lower surface, while the SAP2 have the plasma arrays over their upper surface. The model is 200 mm in span l, 200 mm chord c with two elliptical endplates 300×400 mm to provide a 2D flow. The holder of 28 mm diameter is mounted to the 3-component strain gauge balance.

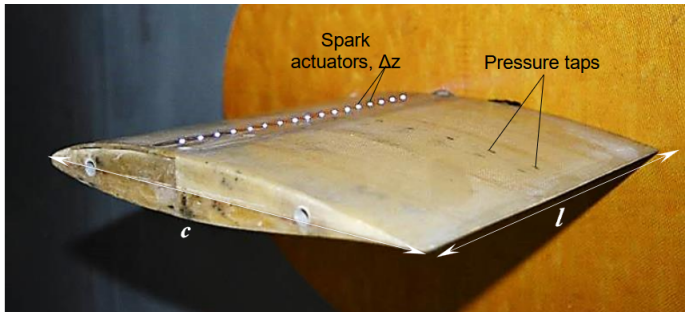

Fig. 7. The SAP2 airfoil model with the ignited spark plasma discharges

The controlled model, endplates, and holders are made of glass-fiber, material with good electro-insulating properties. Pressure distributions along the airfoil are measured using 29 taps. The changeable inserts were made with an array of spark

plasma actuators with the possibility to locate them at different chord positions; Figs. 6b and 7 show the 34% model chord position.

5. Aerodynamic experiment: conditions and results

Present investigations were carried out in a range of Reynolds numbers by the model chord, $\mathrm{Re}_c = (0.3 \div 0.7) \times 10^6$. The SAP2 model was controlled with the $\Delta z = 4$ mm pulsated multi-spark array located at 34% of the cord over the airfoil upper surface.

5.1. Aerodynamic characteristics of the controlled airfoil at $\mathrm{Re}_c = 0.3 \times 10^6$

Here, measurement results are discussed for the range of angles of attack $\alpha = 10 \div +19^\circ$, free-stream velocity, $U_0 = 22.5$ m/s, and varying control parameters, such as duration τ, ms and repetition rate F, Hz of pulsated plasma discharges that directly characterize the energy deposited in the flow.

Lift and drag coefficients measured for the controlled model are shown in Figs. 8, 9. The curves marked 'Ref.' are the baseline cases with no flow control applied. Denotations of the "0.2/200" type refer to the combination of the pulse duration in milliseconds (0.2) with the pulse repetition rate in Hertz (200).

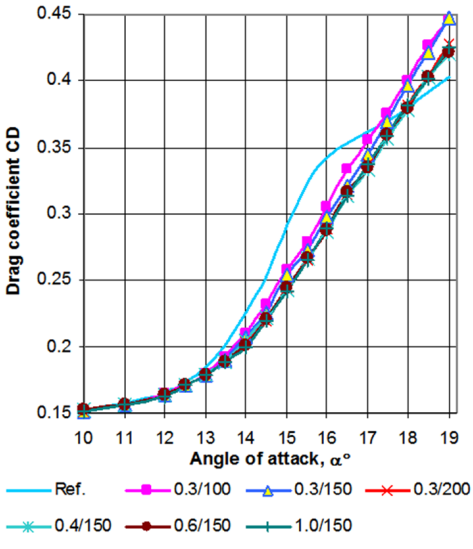

Fig. 8. Drag coefficient vs. angle of attack

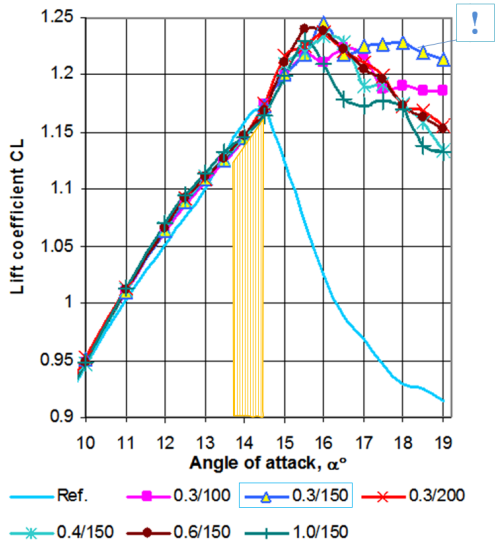

Fig. 9. Lift coefficient vs. angle of attack

At low angles of attack up to the pre-stall region, the discharges have a negligible effect on lift and drag. In the pre-stall region, all lift curves are very close to each other and diverge after the baseline stall angle is reached. The lift coefficient in the controlled case starts growing from $\alpha = 10^\circ$ Depending on the combination

of pulse duration/repetition rate, different increments for lift coefficient and stall angle were found.

The drag coefficient decreases in the controlled case in the range of $\alpha \approx 12^\circ$ (near-critical angle of attack of the baseline case) to $\alpha = 17.5 \div 18.5^\circ$ (baseline post-stall region). However, as the angles of attack grow further, it increases faster than in the baseline case. At the controlled stall angle $\alpha = 16^\circ$, the drag coefficient decrement is $\Delta C_{D\alpha=16.0^\circ} \approx 5.6\%$ for $\tau/F = 0.4/150$.

The close value of τ/F, $\tau = 0.3$ ms, $F = 150$ Hz, is an optimal combination for $\alpha = 14.5 \div 16^\circ$, providing the maximal lift increment, $\Delta C_{L\,max}$ of 8.5% and the stall angle increment, $\alpha_{stall} = 1.5 \sim 2.0^\circ$. This case is made bold in Table 1. It should be mentioned that these conditions do not correspond to maximal energy deposited in the flow, as it is shown in Table 1. This is because, for the considered conditions, the obtained favorable effects result not only from the energy deposited in the flow by plasma discharges. For example, the increments of lift coefficient and stall angle for the case of $\tau/F = 0.3/150$ are lower than those for the more powerful 0.6/150 and 1.0/150 modes.

Table 1. Electromagnetic flow control parameters and the total discharge power

Pulse duration τ, ms	Pulse repetition rate, F, Hz	Full discharge power, W
0.3	100	24
0.3	**150**	**28**
0.3	200	39
0.4	150	31
0.6	150	39
1.0	150	67

The maximal lift coefficient under controlled conditions at the stall angle of $\alpha = 16.0^\circ$ is 22% greater than the baseline C_L at this angle of attack. More than that, an abrupt lift drop in the baseline case turns into a much smoother lift decline in the post-stall region in the controlled case.

5.2. Pressure redistribution along the airfoil

A series of pressure measurements along the airfoil chord allow us to interpret the nature of the observed variations of drag and lift in the controlled case. Pressure distribution over the model is shown in Fig. 10 for the near-critical angle of attack in the baseline case, $\alpha = 14^\circ$. The measured relative pressure values characterize considerable suction growth over 5% of the model front part. It is directed mainly forward, thus resulting in a noticeable drag reduction. It is accompanied by a suction loss in the model aft part along approximately 15% of its chord which is almost normal to the flow direction. As a result, an insignificant lift drop takes place in the area of $\alpha = 13.5^\circ \div 14.5^\circ$ marked yellow in Fig. 9.

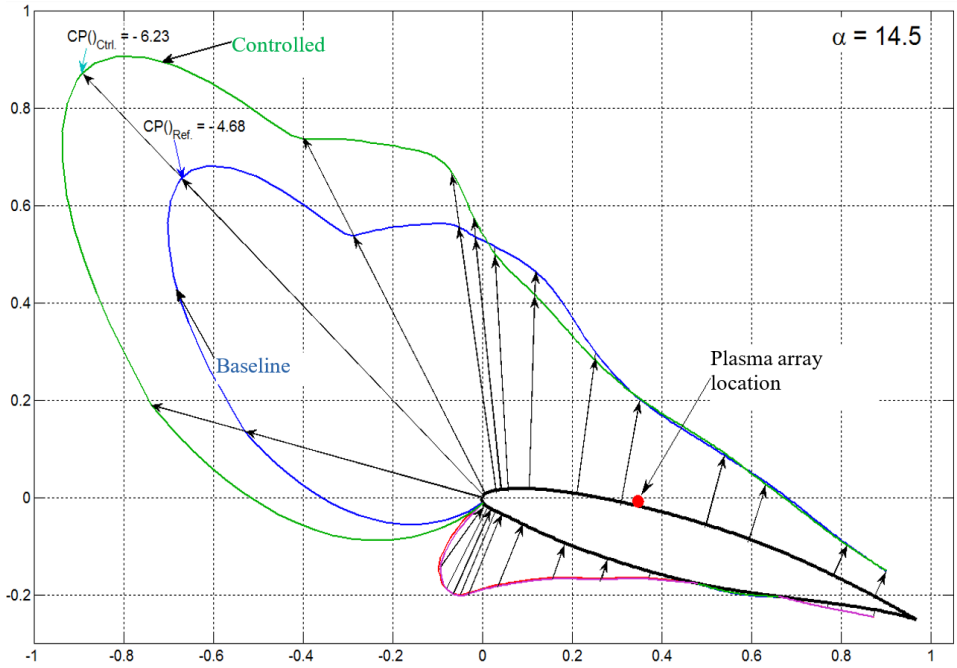

Fig. 10. Pressure distribution over SAP2 model with plasma array located at 34% of chord: $\alpha = 14.5^{\circ}$, $\tau = 0.4$ ms, $F = 150$ Hz

To illustrate the selective character of plasma array impact on the stall and post-stall areas which are referred to in the baseline case, Fig. 11 shows pressure redistributions around the model for the case of the plasma array located closer to the leading edge at 14.9% of the chord. The same control conditions were set for all three considered series of angles of attack varying from 14° (i.e., around a critical angle in the baseline case) to post-critical angles growing to 16° and 18.5°, thus showing a new, critical angle of attack in the controlled case.

For a more comprehensive picture of flow modification by the designed array of discreet plasma discharges, Fig. 12 presents aerodynamic coefficients for the case of the array mounted at a different location, 14.9% of chord. On the whole, it shows an obvious performance improvement.

5.3. Increments of aerodynamic characteristics of the controlled airfoil depending on Reynolds number, $\mathbf{Re_c = (0.3 \div 0.7) \times 10^6}$

The favorable effects of the controlled plasma discharges on flow characteristics can be better understood by focusing on the produced changes of drag and lift depending on Reynold number. Figs. 13–18 show the results for the plasma array with $\Delta z = 4$ mm scaling mounted at 24.5% of chord, i.e., between the locations of

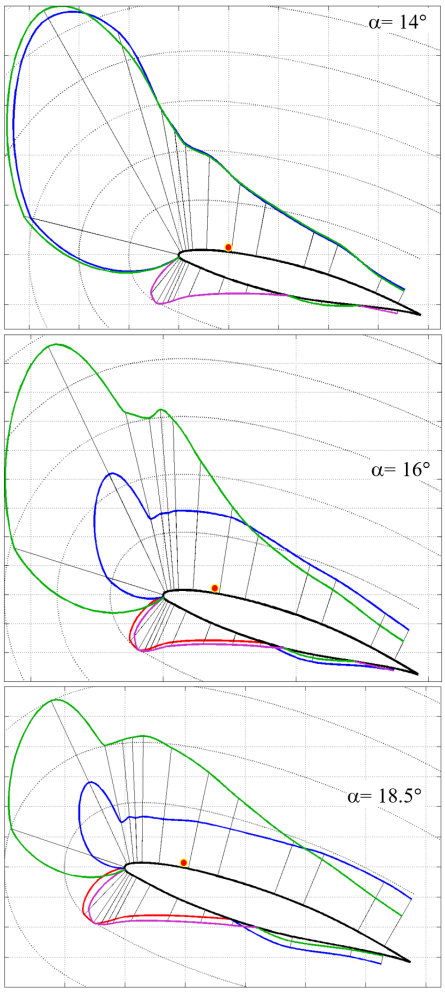

Fig. 11. Pressure distribution over SAP2 model with plasma array located at 14.9% of chord: τ = 0.3 ms; F = 125 Hz

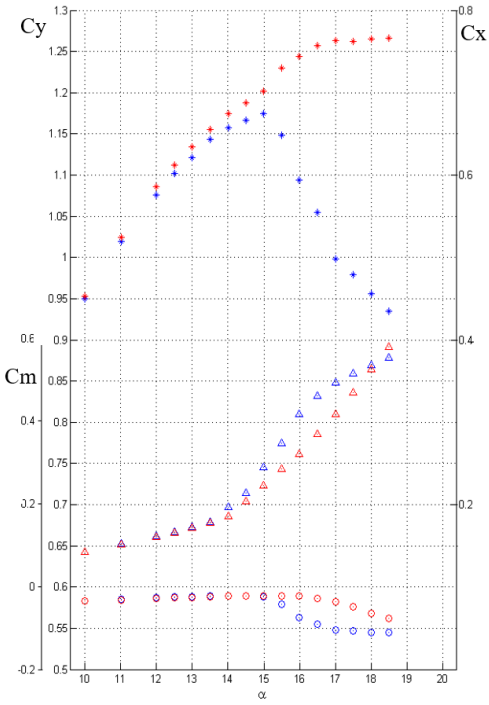

Fig. 12. Aerodynamic coefficients of pitch moment Cm (1st left vertical axis) – circular dots, lift Cy – cross-shaped dots (2nd left vertical axis), and drag Cx – triangular dots (right vertical axis) depending on angle of attack; blue dots – baseline case, red dots – controlled case; SAP2 model with plasma array located at 14.9% of chord, τ = 0.3 ms; F = 125 Hz

the cases considered above. Marked yellow are the ranges of angles of attack for three Reynolds numbers where drag decrements and lift increments were found.

The analysis of the obtained results shows that the airfoil aerodynamic characteristics are sensitive to the energy deposited in the flow, which in turn is proportional to the pulse duration and repetition rate of generated plasma discharges. With growing energy of disturbances, both the drag reduction value and the range of angles of attack where it takes place grow for all tested Reynolds numbers. Maximum drag reduction of 7% was found for $\mathrm{Re_c} = 0.5 \times 10^6$ (Fig. 15). It can be explained by comparing drag variation in the baseline and the controlled cases

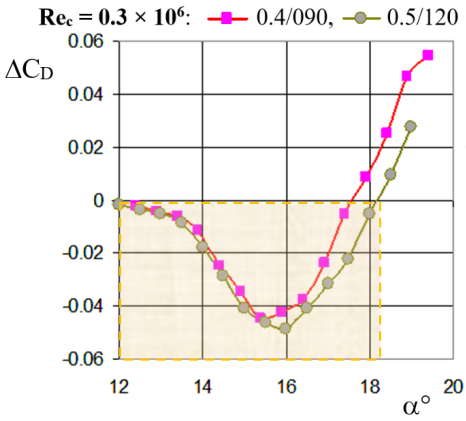

Fig. 13. Drag coefficient vs. angle of attack

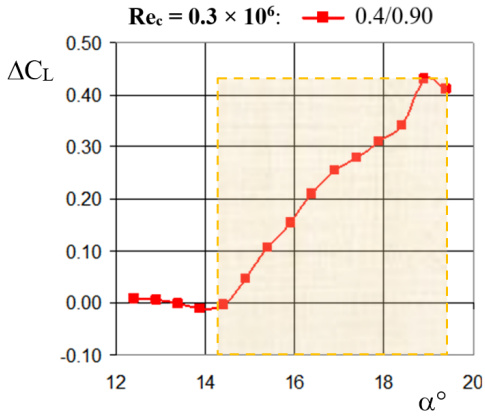

Fig. 14. Lift coefficient vs. angle of attack

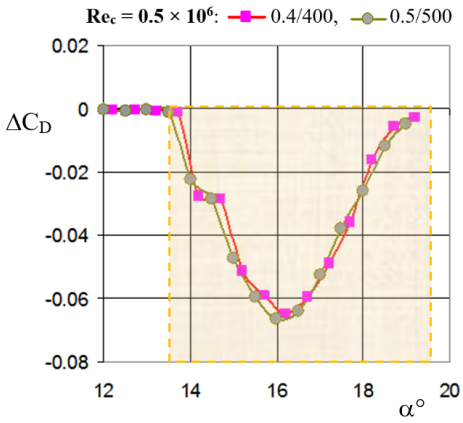

Fig. 15. Drag coefficient decrement depending on angle of attack

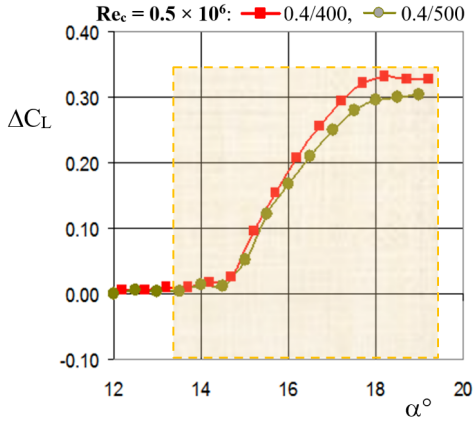

Fig. 16. Lift coefficient increment depending on angle of attack

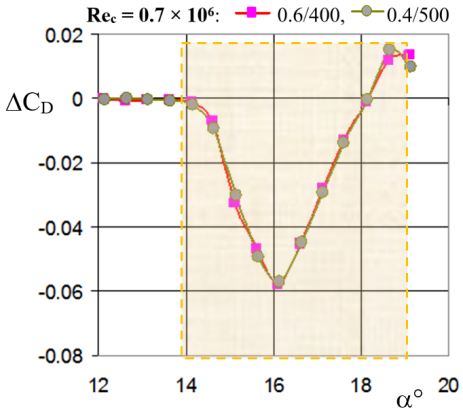

Fig. 17. Drag coefficient decrement depending on angle of attack

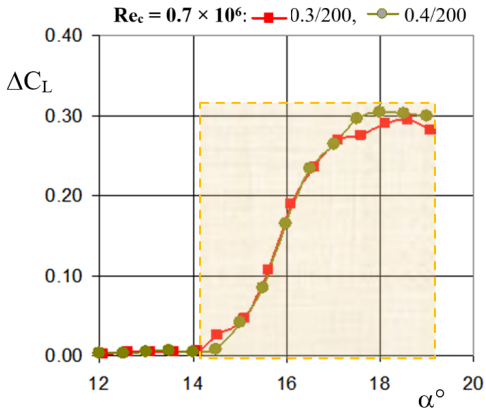

Fig. 18. Lift coefficient increment depending on angle of attack

after $\alpha \approx 14^\circ$ in Fig. 8; it shows the enlarged angles of operation for the controlled cases up to 17–18.5°.

This particular area of angles of attack shows a growth of lift compared to the lift rapidly falling in the baseline case (Fig. 9). However, despite the fact that ΔC_L grows by 30-40% (Figs. 14, 16, 18), only the control mode, like the one of $\tau/F = 0.3/150$ in Fig. 9, may have practical importance. It is represented by the blue curve above $C_L = 1.2$, which indicates the conditions acceptable for the stable flight. Unlike drag, lift appears to be more affected by the energy of generated disturbances that is indicated by the divergence of curves in Figs. 16, 18 for different values of pulse duration and repetition rate. A search of optimal configurations for a given Re_c requires a broader investigation focused on variation of all control parameters and their combinations.

6. Conclusions

The developed concept of energy-efficient flow control based on smart flow-scale restructuring was tested for a wing with an apriori known streamlined shape. Here, the advantage of providing active flow control is supplemented with the control flexibility due to the application of pulsating spark plasma discharges characterized by a number of electromagnetic parameters. The method makes it possible to maintain the surface smooth, without deteriorating its initial shape. Optimal control conditions for a given Reynolds number are sought after by varying pulsating plasma parameters and the chordwise location of the vortex-generator array on the airfoil, as well as a distance between the neighboring discharges in the array that defines the scale of generated disturbances.

It was found that the supercritical airfoil could be successfully controlled at low Re regimes under the conditions of growing angle of attack. For example, the results obtained under controlled conditions show that

- the stall angle grows by 1.5–3.5° depending on the pulsating plasma parameters and the total energy deposited in the flow by plasma discharges;
- there is a possibility to increase lift coefficients within the range of baseline stall and post-stall angles of attack by $\Delta C_{L\,max} \approx 5$–10%;
- drag is reduced in the post-stall region, e.g., $\Delta C_{D\alpha=16.0^\circ} \approx 7.0\%$.

Acknowledgments

This material is based upon work supported by the European Office of Aerospace Research and Development, AFOSR, AFRL under the CRDF GAP grant # UKE2-1518-KV-07.

The authors acknowledge with thankfulness the contributions of Dr. Vyacheslav Boretsky and his team for the professional development of the plasma generation system according to the aerodynamic requirements, Drs. Mark Maurice and

Julian Tishkoff for their permanent supportive interest, motivating and encouraging discussions.

References

[1] N. Yurchenko and V. Babenko. On stabilization of streamwise vortices by the dolphin skin. *Biophysics*, 25(3):229–304, 1980. (in Russian).

[2] S.F. Hoerner. *Aerodynamic Drag: Practical Data on Aerodynamic Drag Evaluated and Presented*. Otterbein Press, University of Minnesota, 1951.

[3] X. Pu, G. Li, and H. Huang. Preparation, anti-biofouling and drag-reduction properties of a biomimetic shark skin surface. *Biology Open*, 5(4):389–396, 2016. doi: 10.1242/bio.016899.

[4] A.R. Karabetça. Using biomimicry as a design strategy. In: *Proceedings Book, AIOC'15 International Conference on New Trends in Architecture and Interior Designing*, Dubai, March 2015.

[5] N. Yurchenko, A. Pedishius, G. Zygmantas, and S. Yapertas. Heat transfer in a turbulent boundary layer with embedded longitudinal vortices, *Energetika Journal*, 3(178), 1990.

[6] K.-S. Choi and S. Hamid. Heat transfer study of riblets. In K.S. Choi (ed): *Recent Developments in Turbulence Management. Fluid Mechanics and Its Applications*, Vol. 6, Springer 1991. doi: 10.1007/978-94-011-3526-9_2.

[7] P. Vilkinis, J. Šereika, N. Pedišius, and G. Zygmantas. Experimental study of flows over triangular riblets in cavity-like geometry. *Experimental Thermal and Fluid Science*, 134:110621, 2022. doi: 10.1016/j.expthermflusci.2022.110621.

[8] M. Walsh. Turbulent boundary layer drag reduction using riblets. In: *20th Aerospace Sciences Meeting*, AIAA 1982-169, 1982. doi: 10.2514/6.1982-169.

[9] D. Bushnell. Turbulent drag reduction for external flows. In: *21st Aerospace Sciences Meeting*, AIAA 1983-227, 1983. doi: 10.2514/6.1983-227.

[10] Y. Li, H. Mao, P. Hu, et al. Bioinspired Surfaces: Bioinspired Functional Surfaces Enabled by Multiscale Stereolithography. *Advanced Materials Technologies*, 4(5):1970030, 2019. doi: 10.1002/admt.201970030.

[11] A. Chavarin and M. Luhar. Resolvent analysis for turbulent channel flow with riblets. *AIAA Journal*, 58(2):1-11, 2020. doi: 10.2514/1.J058205.

[12] N. Yurchenko. Research strategy for active flow control based on distributed thermal fields. *International Journal of Fluid Mechanics Research*, 37(5):470–489, 2010. doi: 10.1615/InterJFluidMechRes.v37.i5.70.

[13] N. Yurchenko and J. Delfs. Optimal control of boundary layers under body forces. In H.F. Fasel, W.S. Saric (eds):*Laminar-Turbulent Transition. IUTAM Symposia*, Springer 2000. doi: 10.1007/978-3-662-03997-7_47.

[14] N. Yurchenko and R. Rivir. Improvement of the turbine blade performance based on the flow instability and receptivity analysis. In *8th International Symposium on Transport Phenomena and Dynamics of Rotating Machinery*, pages 300-306, Honolulu, Hawai, USA,26-30 March 2000.

[15] K. Hanjalic and B. Launder. *Modeling Turbulence in Engineering and the Environment*. Cambridge University Press, 2011. doi: 10.1017/CBO9781139013314.

[16] N. Yurchenko. MW-generated point plasma discharges as a novel approach to boundary-layer control. In *46th AIAA Aerospace Sciences Meeting and Exhibit*, AIAA 2008-1388, 2008. doi: 10.2514/6.2008-1388.

[17] N. Yurchenko, P.Vynogradskyy,and K.Kuzmenko. Flow response to multi-spark and multi-jet flow actuation, In *54th AIAA Aerospace Sciences Meeting*, AIAA 2016-1819, 2016. doi: 10.2514/6.2016-1819.

[18] Q. Liu and Y. Zhang. Shock wave generated by high-energy electric spark discharge. *Journal of Applied Physics*, 116(15):153302, 2014. doi: 10.1063/1.4898141.

[19] B. Singh, L.K. Rajendran, M. Giarra, P.P. Vlachos, and S.P.M. Bane. Measurement of the flow field induced by a spark plasma using particle image velocimetry. *Experiments in Fluids*, 59(12):179, 2018. doi: 10.1007/s00348-018-2632-y.

[20] O.I. Vishnyakov, P.A. Polivanov, A.A. Sidorenko, and A.D. Budovsky. Development of disturbances generated by an electric discharge in the shock wave/boundary layer interaction zone. *Thermophysics and Aeromechanics*, 30:673—681, 2023. doi: 10.1134/S0869864323040078.

[21] H. Jois, A.S. Hong, and P.J. Ansell. High-lift aerodynamics of integrated distributed propulsion systems with thrust vectoring. *Journal of Aircraft*, 2024. doi: 10.2514/1.C037902.

[22] P. Vynogradskyy, N. Yurchenko, R. Pavlovskyy, A. Zhdanov, M. Lazarjan, Y. Paramonov, I. Esakov, and A. Ravaev. Boundary-layer control based on localized plasma generation: wind-tunnel investigations. In *48th AIAA Aerospace Sciences Meeting Including the New Horizons Forum and Aerospace Exposition*, AIAA 2010-1007, 2010. doi: 10.2514/6.2010-1007.